# Metallic Nanodot Arrays by Stencil Lithography for Plasmonic Biosensing Applications

**Oscar Vazquez-Mena,[†,*] Takumi Sannomiya,[‡] Luis G. Villanueva,[†] Janos Voros,[‡] and Juergen Brugger[†,*]**

[†]Microsystems Laboratory, Ecole Polytechnique Fédérale de Lausanne (EPFL), 1015 Lausanne, Switzerland, and [‡]Laboratory of Biosensors and Bioelectronics, Eidgenössische Technische Hochschule Zürich (ETHZ), 8092 Zurich, Switzerland

**ABSTRACT** The fabrication of gold nanodots by stencil lithography and its application for optical biosensing based on localized surface plasmon resonance are presented. Arrays of 50−200 nm wide nanodots with different spacing of 50−300 nm are fabricated without any resist, etching, or lift-off process. The dimensions and morphology of the nanodots were characterized by scanning electron and atomic force microscopy. The fabricated nanodots showed localized surface plasmon resonance in their extinction spectra in the visible range. The resonance wavelength depends on the periodicity and dimensions of the nanodots. Bulk refractive index measurements and model biosensing of streptavidin were successfully performed based on the plasmon resonance shift induced by local refractive index change when biomolecules are adsorbed on the nanodots. These results demonstrate the potential of stencil lithography for the realization of plasmon-based biosensing devices.

**KEYWORDS:** stencil lithography · shadow mask · nanofabrication · nanodots · plasmonics · biosensors

Nanotechnology has enabled new developments and possibilities for biology and biomedical applications. Among them, the use of localized surface plasmon resonance (LSPR) in metallic nanostructures has been demonstrated as a novel method for biomolecular sensing.[1−4] LSPR is the optical resonance in electromagnetic radiation due to the coupling with electrons (plasmons) in nanoscale metallic structures.[5−7] The resonance wavelength depends not only on the material and geometry of the nanostructures but also on the refractive index of the surrounding media. LSPR is used for label-free biosensing by monitoring the resonance wavelength, which follows the changes in local refractive index due to the adsorption of biomolecules on the nanostructures. The use of LSPR for biosensing has important advantages: the detection system is based on simple and low-cost transmission spectroscopy;[8,9] the metallic nanodots do not blink or bleach; and sensitivities comparable to other state of the art methods can be achieved in a small detection area.[1,10−12]

However, similar to other nanoscale phenomena, the application of this technology still requires adequate and affordable nanofabrication methods for further development and low-cost production. Chemically synthesized nanoparticles are extensively used for LSPR biosensing, yet the positioning of the nanoparticles is still a major challenge for the integration and device fabrication using this bottom-up approach.[2,13] Metallic nanodots for biosensing have also been produced using conventional but expensive nanopatterning methods such as electron beam lithography[14,15] and extreme ultraviolet interference lithography.[16] Alternative methods for low-cost nanopatterning such as nanoimprint lithography[17,18] and nanosphere lithography[19,20] have been also successfully used for the fabrication of metallic nanostructures. However, these methods also have limitations, such as the use of resists and lift-off processing.

In this work, we present stencil lithography as an alternative method to fabricate metallic nanodots for label-free LSPR biosensing. Stencil lithography is based on the principle of shadow mask patterning for local modification or deposition on a substrate, as shown in Figure 1.[21−23] This technique has been employed not only for material deposition but also for etching[24] and implantation[25] of submicrometer structures. Stencil lithography has been used for the fabrication of metallic nanowires,[26−29] nanodots,[23,30] resonators,[31] and plasmonic structures.[32,33] Recently, Aksu *et al.* reported the use of stencil lithography for infrared plasmonic nanorods.[33] Herein we focused on nanodots down to 50 nm for label-free LSPR biosensors. Stencil lithography does not require any resist processing such as coating, baking, solvents, or energy radiation. It also offers great versatility regarding the materials and substrates that can be

*Address correspondence to oscar.vazquez@epfl.ch, juergen.brugger@epfl.ch.

Received for review August 5, 2010 and accepted December 16, 2010.

**Published online December 30, 2010**
10.1021/nn1019253

© 2010 American Chemical Society

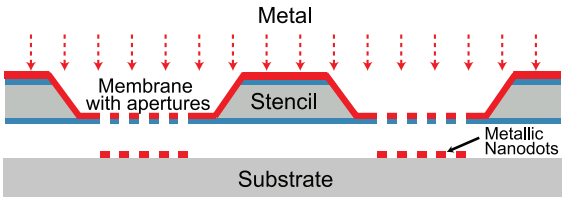


**Figure 1. Stencil lithography. A stencil containing membranes with apertures is fixed on top of a substrate. Then, during the evaporation of a metal, the material passing through the stencil is deposited on the substrate, reproducing the pattern of the stencil apertures.**

deposited and patterned. The patterns defined by stencil lithography can have different shapes and distribution; they are not limited to spherical related geometries and do not require any lift-off processing as compared to nanosphere or colloidal lithography.[19,20,34] Stencils can also be reused several times, allowing the cost-efficient fabrication of nanostructures.[26,33,35,36] On the other hand, stencil lithography still faces challenges for the fabrication of nanostructures:[37] the fragility of the membranes, the clogging due to material accumulation in the apertures,[35] and the blurring that limits the resolution of the deposited structures.[38] Various approaches and solutions have been proposed for these issues as discussed elsewhere.[35,39−42]

This work reports the fabrication of 50−200 nm size gold nanodots deposited on silicon and glass substrates. The structures are analyzed by scanning electron microscopy (SEM) and atomic force microscopy (AFM). The localized surface plasmon resonances of the Au nanodots deposited on glass wafers are investigated through their extinction spectra. To study the sensing capabilities of the stenciled nanodots based on LSPR, the bulk sensitivity to the refractive index is measured. Finally, 100 nm nanodots are successfully used for biosensing, showing a wavelength shift of the LSPR peak upon the binding of biotin and streptavidin.

## RESULTS AND DISCUSSION

**Nanodot Deposition.** The stencils consist of silicon chips supporting low stress silicon nitride (LS SiN) membranes with micro- and nanoapertures. For the deposition of the nanodots, stencil chips of 6 × 6 mm$^2$ in size and 525 $\mu$m in thickness were fabricated. The stencils contain LS SiN membranes 230 × 300 $\mu$m$^2$ in size and 100 nm in thickness patterned with arrays of nanoholes. The arrays have sizes between 20 × 20 and 40 × 40 $\mu$m$^2$. The stencil nanoholes have widths ($W_{St}$) of 50, 75, 100, 150, and 200 nm and were defined by electron beam lithography and silicon nitride dry etching. The holes were designed as squares. For each nanohole size, different arrays with interhole spacing ($S$) of 50, 75, 100, 150, 200, and 300 nm were produced. The nanoholes in the stencils were inspected by SEM and show variations in size of ±8 nm (two times the standard deviation $\sigma$). In the case of the 50 nm

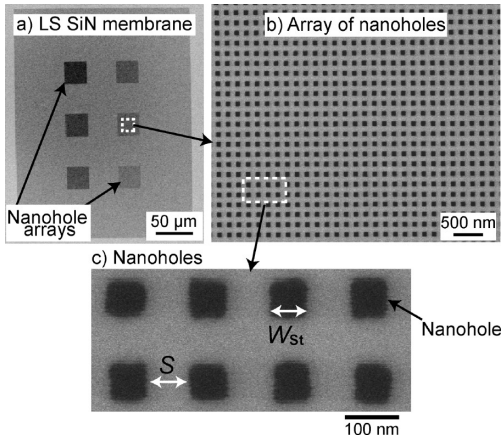


**Figure 2. Stencil for nanodot deposition. (a) SEM micrograph of a LS SiN stencil membrane with an area of 230 × 300 $\mu$m$^2$ and a thickness of 100 nm. The membranes have 6 arrays of nanoholes with different nanohole spacing (50−300 nm). This membrane has arrays with 75 nm wide nanoholes, and the size of the arrays is 30 × 30 $\mu$m$^2$. (b) Magnified SEM micrograph of an array of nanoholes with width of $W_{St}$ = 75 nm and spacing of $S$ = 75 nm (pitch = 150 nm). (c) Zoom-in on the 75 nm wide nanoholes defining $W_{St}$ (nanohole width) and $S$ (nanohole spacing).**

wide nanoholes, their shape is rounded due to the limitations of the electron beam lithographic process. The process flow for the fabrication of the stencils is shown in the Supporting Information, Figure SI1. Figure 2 shows a SEM image of a stencil membrane with several nanohole arrays and magnified SEM images of an array of 75 nm wide nanoholes with interhole spacing of 75 nm.

To fabricate the nanodots, the stencil chips were fixed on Si and glass substrates with adhesive tape. The fixation of the stencil to the substrate is schematically illustrated in the Supporting Information in Figure SI2. Then, 5 nm of Ti was deposited through the stencil as adhesion layer followed by 45 nm of Au. The depositions were done by electron beam evaporation at a pressure of $10^{-6}$ mbar, room temperature, and deposition rates of 4 Å/s for Ti and 1 Å/s for Au. The depositions were carried in a Leybold LAB-600 evaporator having a source−substrate distance of $D$ = 1 m and a material source with diameter of $S_M \sim 5$ mm. After the deposition, the stencil apertures are clogged, reducing their size or closing them completely. The stencils can be cleaned and reused several times using wet etching solutions to remove Ti and Au as described in previous reports.[26,33,35,36]

When the stencil is fixed on the substrate and during the metal deposition, there is an inherent gap between the stencil and the substrate that is due to several factors such as the curvature of the wafers and chips, the topography of their surface, and any bending of the membranes. Conventional silicon wafers used as stencils or substrates always have a slight curvature that results in a small gap between the stencil and the substrate, as shown in the Supporting

Information in Figure SI3. This stencil–substrate gap, together with the surface diffusion of the material during the deposition, produces the blurring phenomenon

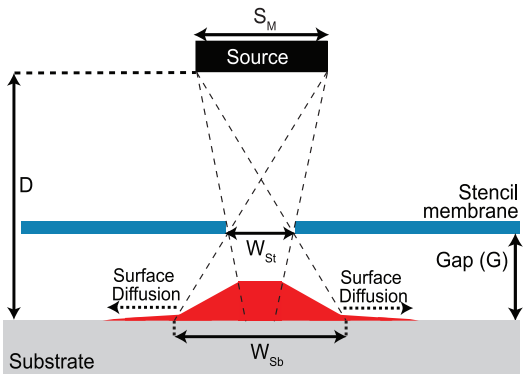


**Figure 3. Blurring is the size enlargement of the deposited structures with respect to the stencil aperture ($B = W_{Sb} - W_{St}$). The blurring is due to the geometrical configuration of the source stencil–substrate setting, to the divergent flow of metal vapor from source to substrate and to the surface diffusion of the deposited material on the substrate. The blurring also produces a spread shape on the deposited structures. The geometrical contribution to the blurring can be approximated to $B = W_{Sb} - W_{St} \approx G \times S_M/D$.**

known in stencil lithography, as illustrated in Figure 3 and discussed in detail elsewhere.[26,37,38,43] The blurring produces a size enlargement of the deposited structures with respect to the size of the stencil apertures and a spread shape on the deposited structures. From previous studies on stencil lithography, it is known that the size enlargement of the structures, $B = W_{Sb} - W_{St}$, can be estimated as $B \approx G \times S_M/D$ (see Figure 3), where $G$ is the size of the stencil–substrate gap.[37,38] In our case, for $6 \times 6$ mm$^2$ stencil chips fixed on the substrate wafer, the gap observed between the stencil and the substrate is usually smaller than 5 $\mu$m. Considering $D = 1$ m and $S_M = 5$ mm, it can be estimated that the size enlargement of the structures $B$ will be less than 25 nm.

Arrays of Au nanodots with sizes of $W = \sim$50, $\sim$75, $\sim$100, $\sim$150, and $\sim$200 nm and with different spacing $S$ from 50 to 300 nm were deposited on Si and glass substrates using stencils with the corresponding aperture geometry. In this case, the arrays are $30 \times 30$ $\mu$m$^2$ in size. SEM measurements were performed to analyze the size and resolution of the nanodots deposited on Si substrates. Figure 4 shows SEM images of 50, 100, and 200 nm wide nanodots with their corresponding

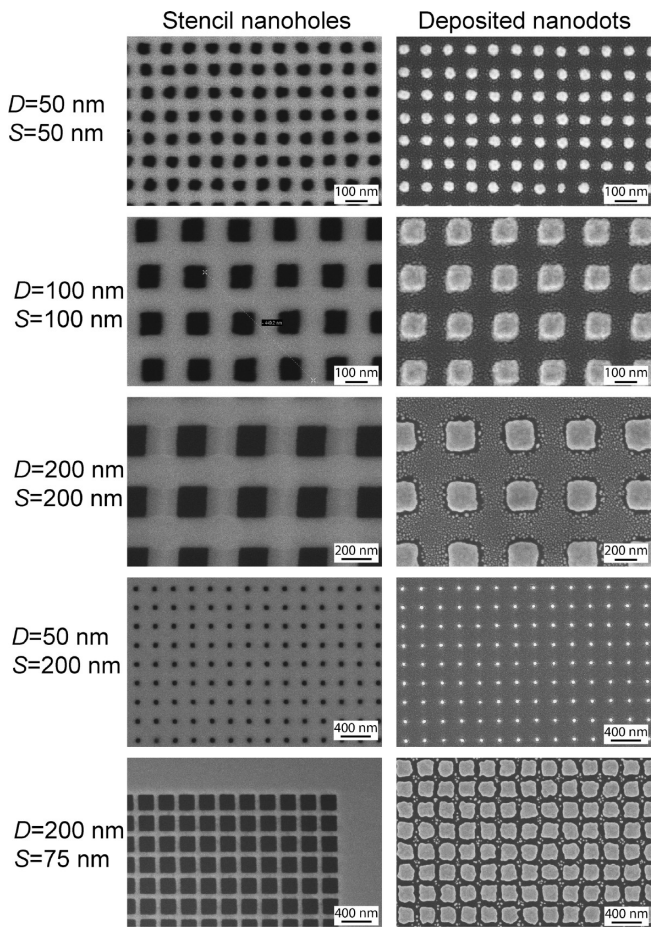


**Figure 4. SEM images of stencil nanoholes and their corresponding Au nanodots with different widths ($W$) and spacing ($S$) deposited on Si substrates. The deposited nanodots reproduce the geometry of the stencil apertures obtaining nanodots down to 50 nm. Due to the blurring and surface diffusion, the size and shape of the deposited nanodots differ from those of the stencil nanoholes. The presence of scattered particles between the nanodots is also due to surface diffusion.**

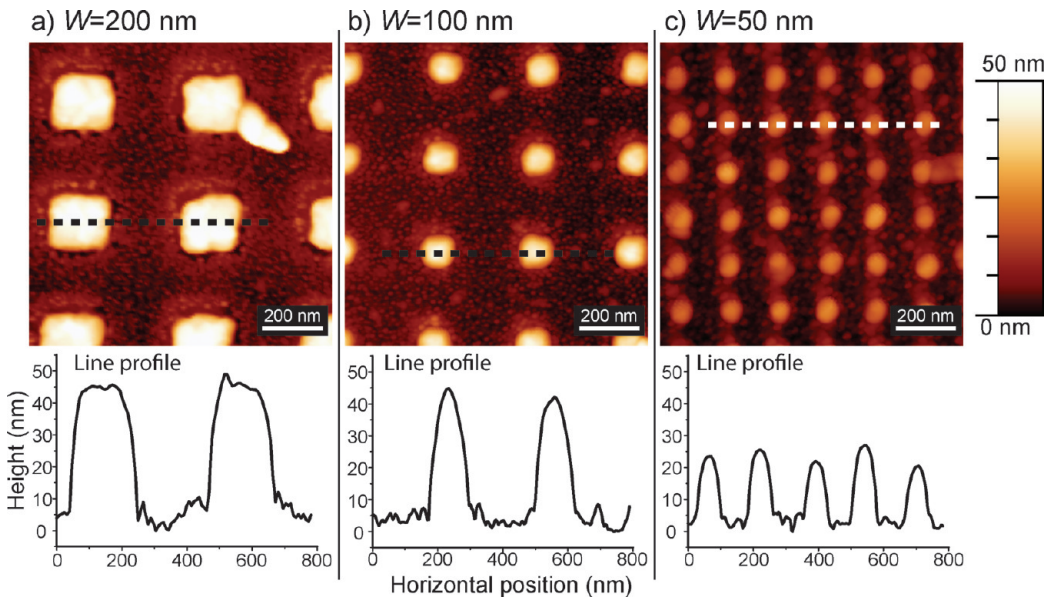


**Figure 5. AFM images and line profiles of Au nanodots deposited on glass wafers: (a) $W = 200$ nm, $S = 200$ nm; (b) $W = 100$ nm, $S = 200$ nm; (c) $W = 50$ nm $S = 100$ nm. The position of the line profile is indicated by the dashed lines in the AFM images. The 50 nm nanodots are thinner compared to the 200 and 100 nm wide nanodots. The AFM images also confirm the presence of scattered particles observed previously in nanodots deposited on silicon wafers (Figure 4).**

stencil apertures. The 50 nm wide nanodots have a rounded shape, whereas the larger 100 and 200 nm wide nanodots keep the squared shape. The nanodots present a size variation of $\pm 10$ nm ($2\sigma$), and on average, they are 10 nm wider than the stencil nanoholes due to blurring. The SEM images in Figure 4 also show the presence of scattered particles between the deposited nanodots due to the blurring and surface diffusion. In the arrays of ~50 nm wide nanodots, such scattered particles are 5−10 nm large, whereas for the ~200 nm wide nanodots, the scattered particles can be as large as 20 nm.

AFM measurements were also performed to analyze the Au nanodots deposited on glass wafers.[44] These measurements confirm the realization of nanodots with dimensions and spacing corresponding to the apertures in the stencil. AFM images also confirm the presence of scattered particles between the nanodots as observed previously on silicon substrates. Figure 5 shows AFM images and line profiles of 50, 100, and 200 nm wide nanodots. The AFM line profiles reveal that the 50 and 75 nm wide nanodots have a reduced thickness compared to the 100, 150, and 200 nm wide nanodots. The profiles in Figure 5 show that the 100 and 200 nm wide nanodots have a thickness between 40 and 45 nm, whereas the 50 nm wide nanodots have a thickness of 20−25 nm. In summary, the SEM and AFM analysis of the stenciled nanodots reveal a good pattern transfer from the stencil to the substrate. However, it also shows the presence of scattered particles and a thickness reduction for the smallest apertures.

The size and shape of the deposited nanodots are affected by the uniformity of the stencil apertures, the blurring related to the stencil−substrate gap, and the surface diffusion properties of Au and Ti. However, it is difficult to differentiate and quantify the contributions of each factor. Au and Ti actually show different behaviors when deposited through stencils due to different surface diffusion and wetting behaviors. The blurring for the Ti adhesion layer is expected to be smaller than for Au since previous reports indicate that the blurring in stencil lithography is also proportional to the deposition thickness,[38] which in this case is nominally 5 nm for Ti and 45 nm for Au. These effects can eventually give rather complicated landscapes because the deposited Au atoms probably have different wetting properties depending on whether they are on top of Ti atoms or on the bare substrate. As seen in SEM and AFM images (Figure 4 and Figure 5), the surface diffusion produces small scattered particles <20 nm in size between the main nanodots rather than a continuous thin film. This is probably a consequence of the wetting properties of Au on silicon oxide. Previously, Tun *et al.* showed that ~20 nm size Au nanostructures deposited through stencils on silicon oxide substrates form droplet-like structures with contact angle larger than 90°.[26] This seems to be reproduced in our experiments, in which the small scattered Au particles show a nonwetting behavior between the dots, where there are probably fewer Ti atoms, as well. The blurring also causes the observed thickness reduction of the structures deposited through the smallest apertures. The effect of the blurring on the thickness of the nanodots is illustrated in the Supporting Information in Figure SI4 and discussed in detail elsewhere.[27,38] The stability of the membranes and the blurring impose the ultimate limit in the density and resolution of

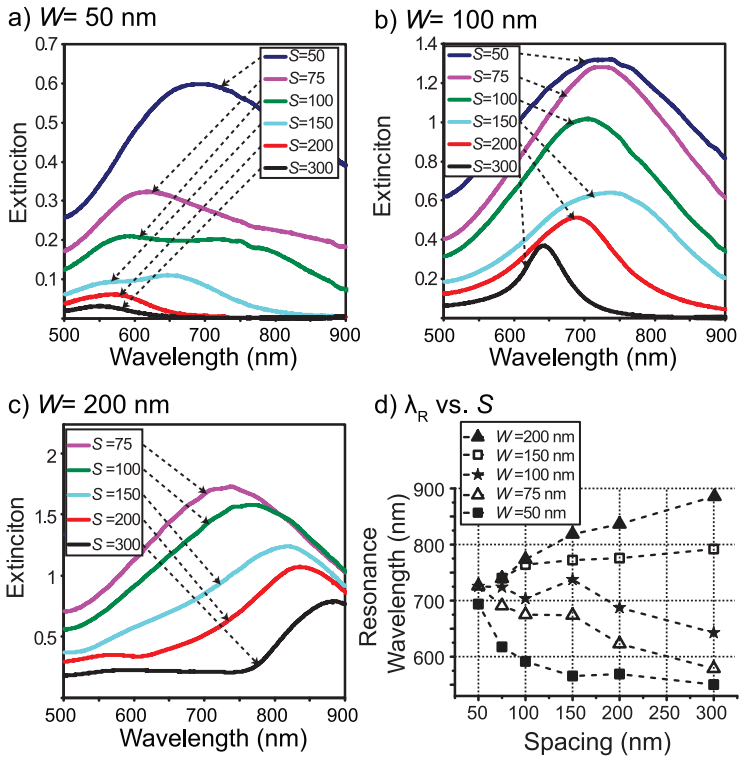


**Figure 6. Extinction spectra of Au nanodots deposited on glass of (a) $W = 50$ nm, (b) $W = 100$ nm, and (c) $W = 200$ nm nanodots with spacing ($S$) from 50 to 300 nm. The resonance peaks for $W = 50$ nm are broad, whereas for $W = 100$ and 200 nm, the resonance is better defined. (d) Resonance wavelength $\lambda_R$ as a function of the nanodot spacing ($S$). For $W = 200$ and 150 nm nanodots, $\lambda_R$ increases with the spacing, while for the smaller $W = 50$ and 75 nm nanodots, $\lambda_R$ decreases with the spacing.**

nanodots that can be achieved by stencil lithography. Figure SI5 of the Supporting Information illustrates these limiting factors for the case of stencils with 150 and 200 nm wide nanoholes with spacing of 50 nm. The use of an improved fixation system would be an important alternative to reduce the blurring and improve the resolution and reproducibility of the dots by minimizing the stencil−substrate gap. The use of compliant membranes has also been demonstrated for reducing the gap and improving the resolution of submicrometer structures deposited through compliant stencils.[41] Concerning surface diffusion, depositions at low temperature are an option to decrease its contribution to the blurring.

**Localized Surface Plasmon Resonance.** The extinction (absorption + scattering) spectra of Au nanodots deposited on a glass substrate were measured in transmission mode. The spectra of $W$ = 50, 100, and 200 nm nanodot arrays with different spacing are shown in Figure 6 ($W$ = 75 and 150 nm Au nanodots spectra are shown in Supporting Information, Figure SI6). These nanodots have resonance wavelengths ($\lambda_R$) in the measured range of 500−900 nm. In the case of the $W$ = 50 nm nanodots, the spectra are very broad (Figure 6a), whereas for larger $W$ = 100 and 200 nm nanodots, the resonance peaks are better defined (Figure 6b,c). This is presumably due to the better defined shapes of the larger nanodots and a larger effect of the blurring for the smaller nanodots. The resonance wavelength $\lambda_R$ of the nanodots depends on their size and spacing. Figure 6d shows the behavior of $\lambda_R$ as a function of the nanodot spacing $S$ for the different nanodot sizes. The plots show that, for the largest 150 and 200 nm nanodots, $\lambda_R$ increases with spacing, whereas for the smallest 50 and 75 nm nanodots, $\lambda_R$ decreases as the spacing increases. The same data for $\lambda_R$ but plotted as function of the size for different spacing are shown in the Supporting Information in Figure SI7.

The observed behavior of the LSPR in the nanodots can be explained by two factors affecting the spectral shift: the interdot coupling is dependent on the dot spacing and the dot shape due to the blurring. Previous works have shown that the shape,[4,45] size,[15] and spacing between the nanodots[14,16,46,47] have an effect on the LSPR of metallic nanodots. In the following arguments, we focus on the interdot coupling to explain the observed dependence of the LSPR wavelength on the dot spacing ($S$). There are two types of interdot coupling affecting the LSPR: (i) the static dipolar interaction, or near-field coupling between the nanodots, that leads to a decrease in $\lambda_R$ (blue shift) as the spacing increases;[16,46] and (ii) the radiative dipolar interaction, or far-field coupling, that increases $\lambda_R$ (red shift) as the spacing increases.[14,47] The radiative dipolar interactions depend on the polarizability of the nanodots and hence on their volume and size.[48] In our case, the $W$ = 150 and 200 nm nanodots showed

an increase of $\lambda_R$ as the spacing increases from 50 to 300 nm. Indeed, the $W$ = 200 nm nanodot arrays showed a stronger spacing dependence ($\sim\Delta\lambda_R/\Delta S \approx$ 0.50) than the $W$ = 150 nm nanodots ($\sim\Delta\lambda_R/\Delta S \approx$ 0.15). Previous works studying radiative dipolar interactions have also shown shifts of $\Delta\lambda_R/\Delta S$ from 0.2 to 0.6 for 100−150 nm size Au nanodots.[14,15,47] These values are comparable to our observations for $W$ = 150 and 200 nm nanodots. Therefore, we conclude that the behavior of our 150−200 nm wide nanodot arrays is mainly dominated by the dipolar radiative (far-field) interactions.

On the other hand, the results for our 50 and 75 nm wide nanodot arrays show an opposite trend. The resonance wavelength decreases rapidly as the spacing between the nanodots is increased. This behavior is mostly related to the near-field coupling, which quickly decays as the separation increases. Since the volume of the smallest $W$ = 50 and 75 nm nanodots is around 1 order of magnitude smaller than the $W$ = 150 and 200 nm nanodots, the polarizability is reduced in the same proportion and the radiative dipolar interaction is strongly reduced. In addition, for the smallest nanodots, the static near-field coupling can be enhanced by the small scattered particles between the nanodots and by the reduced thickness. It is known that particles with elongated shapes show larger near-field coupling than spherical ones.[49,50] Such near-field coupling results in a rapid red shift of the LSPR peak as the interparticle distance decreases.[14,16,46,47] This seems to be clearly the case for the $W$ = 50 nm nanodots, showing a strong red shift when the spacing decreases from 100 to 50 nm. The case for $W$ = 100 nm does not show a clear trend, and probably, there are no clear dominant interactions. Further work is still required to understand the LSPR behavior in the stenciled nanodots. In particular, it would be important to determine the effect of the scattered particles in the plasmon resonance and coupling between the nanodots. Since the absorption and scattering cross section of nanoparticles are proportional to the third and sixth power of the size, it is difficult to observe the resonance from these structures.[6] However, they can play a major role in the near- and far-field coupling between the main nanodots. A full understanding of the plasmons in stenciled nanodots requires more detailed structural analysis, which is a challenge due to the blurring, wetting behavior, and scattered particles of the stenciled structures.

**Sensing Measurements.** In order to demonstrate the biosensing capabilities of the stenciled nanodots, the LSPR response of nanodots deposited on glass to changes in the bulk refractive index and to biotin and streptavidin (SA) was measured. In order to obtain the bulk sensitivity ($m = \Delta\lambda_R/\Delta n$), the extinction spectra of $W$ = 100 nm Au nanodots with 100, 200, and 300 nm spacing were measured in media with different

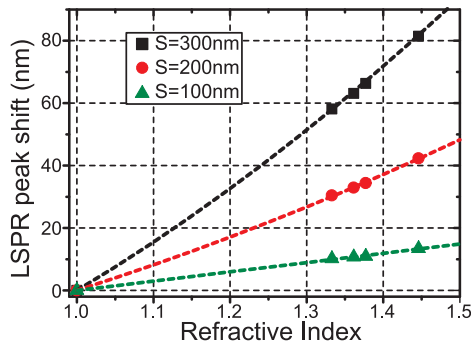


**Figure 7. Bulk sensitivity measurements of $W$ = 100 nm nanodot arrays show the resonance wavelength shift as function of the refractive index ($n$). The measurements correspond to air ($n$ = 1), water ($n$ = 1.33336), ethanol ($n$ = 1.3614), isopropyl alcohol ($n$ = 1.37776), and chloroform ($n$ = 1.4459). The response to the refractive index is larger for larger nanodot spacing. The bulk sensitivities are $m$ = 179 nm/RIU for $S$ = 300 nm, $m$ = 93 nm/RIU for $S$ = 200 nm, and $m$ = 30 nm/RIU for $S$ = 100 nm. The dashed lines show quadratic fittings.**

refractive index. The arrays used in these measurements were 20 × 20, 30 × 30, and 40 × 40 $\mu m^2$ in size for $S$ = 100, 200, and 300 nm interdot spacing, respectively. AFM images of these structures are shown in the Supporting Information in Figure SI8. The used bulk media were water ($n$ = 1.33336), ethanol ($n$ = 1.3614), isopropyl alcohol ($n$ = 1.37776), and chloroform ($n$ = 1.4459).[51] The results for the spectral shift as a function of the refractive index of the liquid media are shown in Figure 7 (the shifts are taken with respect to spectra in air with $n$ = 1). The LSPR wavelength increases monotonously with the refractive index of the media as expected. The bulk sensitivity was found to be higher for larger nanodot spacing. The obtained bulk sensitivities are $m$ = 179 nm/RIU for $S$ = 300 nm, $m$ = 93 nm/RIU for $S$ = 200 nm, and $m$ = 30 nm/RIU for $S$ = 100 nm. The peak shift for $S$ = 300 nm is 6 times larger than that for $S$ = 100 nm. The dashed lines in Figure 7 correspond to a quadratic fitting since $\lambda_R$ is proportional to $n^2$ ($\varepsilon = n^2$) for simple dipoles.[52] However, a linear fit is enough for a good comparison in the given range.[1,4,53]

Higher bulk sensitivity for larger spacing is most likely associated with the spread shape of the dots due to blurring. The spread edge of the nanodots concentrates the enhanced electric field toward the substrate, thus reducing the sensitivity to the bulk medium. The dots with a shorter spacing suffer from this spreading effect more than those with a larger spacing. Two-dimensional simulations of periodic structures with spread edges (instead of 3-D spread dots) indicate a similar trend, higher sensitivity for larger spacing, as shown in Supporting Information in Figure SI9.[54] The stenciled nanodots with a spacing of 300 nm show bulk sensitivities comparable to other similar studies. McFarland *et al.* report $m$ = 191 nm/RIU for an array of nanoparticles fabricated by nanosphere lithography

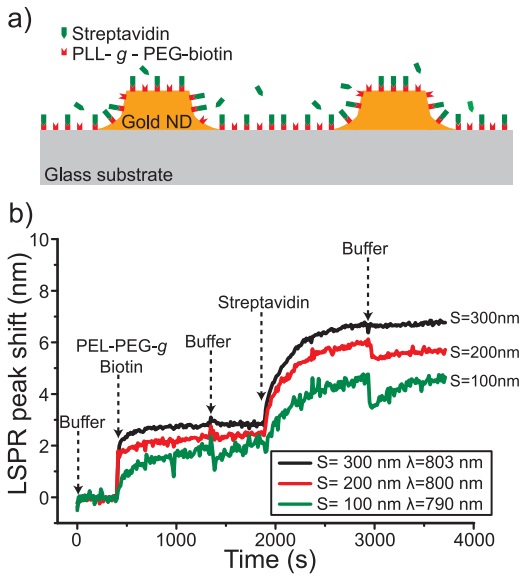


**Figure 8. (a) Schematics illustrating the biosensing system: the PLL-*g*-PEG-biotin attaches to the Au nanodots and to the substrate and then SA binds to the biotin units. (b) Resonance peak shift response (parabolic fitting) in time upon the addition of biomolecules to $W$ = 100 nm Au nanodot arrays with spacing of 100, 200, and 300 nm. The arrows indicate the addition of different solutions. The nanodot arrays show a peak shift upon the addition of PLL-*g*-PEG-biotin and SA (370 nM). The solutions are prepared in a HEPES buffer solution pH 7.4. The spectral shift is larger in the arrays with larger spacing between dots ($\lambda_0$ refers to $\lambda_R$ at the initial baseline measured in HEPES buffer).**

and $m$ = 197 nm/RIU for an individual Ag triangular nanoparticle.[3]

Biosensing measurements of streptavidin (SA) were performed based on the LSPR shift of Au nanodots upon the binding of biomolecules changing the local refractive index. The measurements were done using the same 100 nm wide Au nanodot arrays used for the bulk sensitivity measurements. These measurements were done in a HEPES buffer solution adjusted to pH 7.4. The Au nanodots were first functionalized with a PLL-*g*-PEG-biotin solution (biotinylated poly(L-lysine)-*g*-poly(ethylene glycol), shown in Supporting Information, Figure SI10).[55] During this step, PLL-*g*-PEG-biotin not only binds to the Au nanodots but also to the bare glass substrate between the nanodots. Due to the specific SA−biotin interaction, the SA binds to the Au nanodots and glass substrate *via* the PLL-*g*-PEG-biotin, as shown in Figure 8a. The concentration of the SA solution is 370 nM. The measurements started with the HEPES buffer solution to obtain a baseline. After a few minutes, the PLL-*g*-PEG-biotin solution was injected, producing a first resonance shift. The resonance shift ($\Delta\lambda_R$) response is plotted as a function of time in Figure 8b. The peak shifts (parabolic fitting) are $\Delta\lambda_R \sim$ 1.7 nm for $S$ = 100 nm, $\Delta\lambda_R \sim$ 2.4 nm for $S$ = 200 nm, and $\Delta\lambda_R \sim$ 2.8 nm for $S$ = 300 nm. Half of the peak shift happens within ~15 s, and it takes up to ~10 min to reach the final stable value. The PLL-*g*-PEG-biotin is left incubating until the signal is stabilized and then rinsed with buffer to remove the free PLL-*g*-PEG-biotin left in solution. This buffer rinsing produces a small and transient variation which is an artifact due probably to a small lateral and vertical shift (defocusing) of the sample. This transient variation is more significant for the sample with smaller array area (100 nm spacing, 20 × 20 $\mu m^2$). After a few minutes, the SA solution is injected, generating additional resonance shift in $\lambda_R$. The shift induced by the SA adsorption is $\Delta\lambda_R \sim$ 2.5 nm for $S$ = 100 nm, $\Delta\lambda_R \sim$ 3.4 nm for $S$ = 200 nm, and $\Delta\lambda_R \sim$ 3.8 nm for $S$ = 300 nm. The LSPR response to the SA is larger but slower compared to the PLL-*g*-PEG-biotin. For SA, it takes ~3 min to achieve half of the peak shift and up to ~15 min to reach the final stable value. The slower response for SA compared to the PLL-*g*-PEG biotin has been observed previously.[16] This is presumably due to the lower concentration of SA, as the initial adsorption is limited by diffusion. Finally, the buffer is used to washout nonbound SA causing also a transient variation. Signal-to-noise ratio (S/N) of 92 for SA in the arrays with 300 nm spacing using a measurement area of 40 × 1.5 $\mu m^2$ was obtained based on the 3$\sigma$ of the baseline over 5 min using efficient peak fitting method (CMCC fitting). The spectral shift curves by CMCC fitting method and the behavior of the peak width and height are shown in Supporting Information in Figure SI11. The arrays with 300 nm spacing not only have the largest response but also show a better stability with respect to $S$ = 100 and 200 nm arrays in terms of peak width and quality during the measurements.

Similarly to the bulk sensitivity, the response for both biotin and SA is larger in the arrays with larger nanodot spacing, presumably also due the concentration of the electric field toward the substrate. However, the peak shift response to the biomolecular layer is less dependent on the dot spacing compared to the bulk sensitivity. The peak shift for SA is only 1.5 times larger for $S$ = 300 nm than for $S$ = 100 nm, whereas the bulk sensitivity is 6 times larger. Even though the peak shift value depends on the fitting method, such tendency was observed with different fitting methods. This reduced dependence of the biomolecular adlayer sensitivity on the spacing seems to support our previous hypothesis that the sensitivity is more focused on the substrate. The adsorbed biomolecules, both on nanodots and bare substrate, would probably contribute to the refractive index change more effectively than the case of bulk sensing for all of the spacings. Simulation results of similar 2-D structures, as shown in the Supporting Information in Figure SI9, clearly show the strong field enhancement at the close vicinity of the substrate. The spectral shift curves by CMCC fitting method show comparable performance to other LSPR sensors with small sensing areas.[10,16] The peak shift values obtained are similar to those obtained by Sannomiya *et al.*[16] (SA 370 nM, spectral shift of 6 nm)

and Rashke *et al.*[2] (SA 2 $\mu$M, spectral shift of 2−4 nm) for 40−50 nm Au nanoparticles but using different fabrication methods and nanoparticle geometries. However, our peak shift is lower than that obtained by Haes *et al.*, reporting a shift of 27 nm for 100 nM SA using silver nanoparticles made by nanosphere lithography.[1] Improvements in the plasmonic resonance and biosensing capabilities of the stenciled nanodots can be achieved, reducing the blurring of the deposited structures. This can improve not only the resolution of the dots but also the quality factor of the plasmon resonance increasing the sensitivity of the structures.

## CONCLUSIONS

We have demonstrated a simple fabrication of metallic Au nanodots by stencil lithography and their application for biomolecular detection. Au nanodots down to 50 nm have been achieved; however, the blurring is the major factor affecting the resolution and shape of the dots. The optical measurements show the presence of LSPR in the stenciled Au nanodots. The resonance wavelength behavior depends on their size and spacing and is presumably governed by radiative and near-field interdot coupling. However, the shape of the nanodots and the interdot scattered particles related to the blurring probably also affect the LSPR behavior. The bulk sensitivity and biosensing measurements confirmed that the stenciled nanodots can be used for sensing applications, showing responses comparable to other works that use conventional fabrication methods. The nanodots show larger response for larger interdot spacing. A better understanding of the plasmonic behavior and the sensing response still requires further analysis, which should include the effects of the blurring. Overall, the presented results show the potential of stencil lithography for cost-effective fabrication of metallic nanodots and LSPR-based sensors.

## METHODS

**Stencil Fabrication.** The stencils are fabricated using conventional 100 mm diameter silicon wafers ⟨100⟩ with a 100 nm thick low stress silicon nitride layer deposited by chemical vapor deposition. E-beam lithography and dry etching are used to pattern nanoholes in the silicon nitride. Then, using conventional UV lithography, the backside of the wafer is patterned to form windows for the membrane release. The bulk silicon is etched by deep anisotropic reactive ion etching followed by KOH wet etching. After membrane release, the wafers are cleaved into $6 \times 6$ mm$^2$ chips. The fabrication process in detail is illustrated in Figure SI1 in the Supporting Information.

**Optical Measurements.** The extinction spectra were measured in the 500−900 nm range. The characterization and sensing measurements were performed on the arrays deposited on glass. Extinction spectra were acquired with a spectrophotometer SpectraPro 2150, Pixis 400, Princeton Instruments (USA), equipped with an optical microscope Axiovet 200, Carl Zeiss (Germany). A halogen lamp was used for illumination with nearly zero convergence angle (parallel illumination). A parabolic function was used to detect the resonance wavelength unless otherwise stated.

**Biosensing Measurements.** The biosensing measurements were carried in 160 mM salt buffer solution adjusted to pH 7.4 containing 10 mM of 4-(2-hydroxyethyl)piperazine-1-ethanesulfonic acid (HEPES) with 150 mM NaCl. The Au nanodots were first functionalized with a biotinylated poly(L-lysine)-*g*-poly(ethylene glycol), PLL-*g*-PEG-biotin, shown in the Supporting Information in Figure SI10.[55] The concentration of the PLL-*g*-PEG-biotin solution was 100 $\mu$g/mL. The streptavidin (SA) solution had a concentration of 20 $\mu$g/mL (370 nM). The measurements were done with a flow cell containing the chip with the nanodot arrays. The areas of the sensing measurements for 100 nm size nanodots were $20 \times 1.5$, $30 \times 1.5$, and $40 \times 1.5$ $\mu$m$^2$ for 100, 200, and 300 nm spacing (*S*), respectively. The exposure time at each point in Figure 8b and Figure SI11 in the Supporting Information is 2.5 s.

*Acknowledgment.* This effort was supported by the EPFL-STI Seed Funding and by ETHZ. The authors are very grateful to the EPFL Centre of Micro-Nano-Technology (CMI) and its staff for their effort implementing stencil lithography at CMI. We are also grateful to our colleagues at the Microsystems Laboratory at EPFL for their very valuable support and help.

*Supporting Information Available:* Further information on stencil fabrication, fixation of the stencil to the substrate, effect of wafer curvature on the stencil−substrate gap, thickness reduction, limits in stencil lithography for closely packed structures, extinction spectra, LSPR as function of dot size, AFM images of Au nanodots on glass, 2-D simulations, PLL-*g*-PEG-biotin structure, and resonance peak behavior (peak shift by CMCC method, peak height and peak width) during biosensing experiments. This material is available free of charge *via* the Internet at http://pubs.acs.org.

## REFERENCES AND NOTES

1. Haes, A. J.; Van Duyne, R. P. A Nanoscale Optical Biosensor: Sensitivity and Selectivity of an Approach Based on the Localized Surface Plasmon Resonance Spectroscopy of Triangular Silver Nanoparticles. *J. Am. Chem. Soc.* **2002,** *124*, 10596–10604.
2. Raschke, G.; Kowarik, S.; Franzl, T.; Sonnichsen, C.; Klar, T. A.; Feldmann, J.; Nichtl, A.; Kurzinger, K. Biomolecular Recognition Based on Single Gold Nanoparticle Light Scattering. *Nano Lett.* **2003,** *3*, 935–938.
3. McFarland, A. D.; Van Duyne, R. P. Single Silver Nanoparticles as Real-Time Optical Sensors with Zeptomole Sensitivity. *Nano Lett.* **2003,** *3*, 1057–1062.
4. Anker, J. N.; Hall, W. P.; Lyandres, O.; Shah, N. C.; Zhao, J.; Van Duyne, R. P. Biosensing with Plasmonic Nanosensors. *Nat. Mater.* **2008,** *7*, 442–453.
5. Mie, G. Beiträge Zur Optik Trüber Medien, Speziell Kolloidaler Metallösungen. *Ann. Phys. Berlin* **1908,** *330*, 377–445.
6. Bohren, C. F.; Huffman, D. R. Surface Modes in Small Particles. In *Absorption and Scattering of Light by Small Particles*; John Wiley and Sons, Inc: New York, 1998.
7. Maier, S. A. Localized Surface Plasmons. In *Plasmonics: Fundamentals and Applications*; Springer Science: New York, 2007.
8. Endo, T.; Yamamura, S.; Kerman, K.; Tamiya, E. Label-Free Cell-Based Assay Using Localized Surface Plasmon Resonance Biosensor. *Anal. Chim. Acta* **2008,** *614*, 182–189.
9. Neuzil, P.; Reboud, J. Palm-Sized Biodetection System Based on Localized Surface Plasmon Resonance. *Anal. Chem.* **2008,** *80*, 6100–6103.
10. Dahlin, A. B.; Chen, S.; Jonsson, M. P.; Gunnarsson, L.; Kall, M.; Hook, F. High-Resolution Microspectroscopy of Plasmonic Nanostructures for Miniaturized Biosensing. *Anal. Chem.* **2009,** *81*, 6572–6580.
11. Otte, M. A.; Sepulveda, B.; Ni, W.; Juste, J. P.; Liz-Marzan, L. M.; Lechuga, L. M. Identification of the Optimal Spectral Region for Plasmonic and Nanoplasmonic Sensing. *ACS Nano* **2010,** *4*, 349–357.

12. Svedendahl, M.; Chen, S.; Dmitriev, A.; Kall, M. Refractometric Sensing Using Propagating *versus* Localized Surface Plasmons: A Direct Comparison. *Nano Lett.* **2009,** *9*, 4428–4433.
13. Sannomiya, T.; Hafner, C.; Voros, J. *In Situ* Sensing of Single Binding Events by Localized Surface Plasmon Resonance. *Nano Lett.* **2008,** *8*, 3450–3455.
14. Haynes, C. L.; McFarland, A. D.; Zhao, L.; Van Duyne, R. P.; Schatz, G. C.; Gunnarsson, L.; Prikulis, J.; Kasemo, B.; Kall, M. Nanoparticle Optics: The Importance of Radiative Dipole Coupling in Two-Dimensional Nanoparticle Arrays. *J. Phys. Chem. B* **2003,** *107*, 7337–7342.
15. Bouhelier, A.; Bachelot, R.; Im, J. S.; Wiederrecht, G. P.; Lerondel, G.; Kostcheev, S.; Royer, P. Electromagnetic Interactions in Plasmonic Nanoparticle Arrays. *J. Phys. Chem. B* **2005,** *109*, 3195–3198.
16. Sannomiya, T.; Sahoo, P., K.; Mahcicek, D., I.; Solak, H., H.; Hafner, C.; Grieshaber, D.; Voros, J. Biosensing by Densely Packed and Optically Coupled Plasmonic Particle Arrays. *Small* **2009,** *5*, 1889–1896.
17. Yang, B.; Lu, N.; Huang, C.; Qi, D.; Shi, G.; Xu, H.; Chen, X.; Dong, B.; Song, W.; Zhao, B.; Chi, L. Electrochemical Deposition of Silver Nanoparticle Arrays with Tunable Density. *Langmuir* **2008,** *25*, 55–58.
18. Schvartzman, M.; Nguyen, K.; Palma, M.; Abramson, J.; Sable, J.; Hone, J.; Sheetz, M. P.; Wind, S. J. Fabrication of Nanoscale Bioarrays for the Study of Cytoskeletal Protein Binding Interactions Using Nanoimprint Lithography. *J. Vac. Sci. Technol., B* **2009,** *27*, 61–65.
19. Hulteen, J. C.; Van Duyne, R. P. Nanosphere Lithography: A Materials General Fabrication Process for Periodic Particle Array Surfaces. *J. Vac. Sci. Technol., A* **1995,** *13*, 1553–1558.
20. Klein, M. J. K.; Guillaumee, M.; Wenger, B.; Dunbar, L. A.; Brugger, J.; Heinzelmann, H.; Pugin, R. Inexpensive and Fast Wafer-Scale Fabrication of Nanohole Arrays in Thin Gold Films for Plasmonics. *Nanotechnology* **2010,** *21*, 205301.
21. Ono, K.; Shimada, H.; Kobayashi, S. I.; Ootuka, Y. A New Fabrication Method for Ultra Small Tunnel Junctions. *Jpn. J. Appl. Phys.* **1996,** *35*, 2369–2371.
22. Deshmukh, M. M.; Ralph, D. C.; Thomas, M.; Silcox, J. Nanofabrication Using a Stencil Mask. *Appl. Phys. Lett.* **1999,** *75*, 1631–1633.
23. Brugger, J.; Berenschot, J. W.; Kuiper, S.; Nijdam, W.; Otter, B.; Elwenspoek, M. Resistless Patterning of Sub-Micron Structures by Evaporation through Nanostencils. *Microelectron. Eng.* **2000,** *53*, 403–405.
24. Villanueva, G.; Vazquez-Mena, O.; van den Boogaart, M. A. F.; Sidler, K.; Pataky, K.; Savu, V.; Brugger, J. Etching of Sub-Micrometer Structures through Stencil. *Microelectron. Eng.* **2008,** *85*, 1010–1014.
25. Villanueva, L.; Martin-Olmos, C.; Vazquez-Mena, O.; Brugger, J.; Langlet, P.; Bausells, J.; Monserrat, J. Localized Ion-Implantation through Micro/Nanostencil Masks. *IEEE Trans. Nanotechnol.* DOI: 10.1109/TNANO.2010.2090171.
26. Tun, T. N.; Lwin, M.; Kim, A. H. H.; Chandrasekhar, A. N.; Joachim, C. Wetting Studies on Au Nanowires Deposited through Nanostencil Masks. *Nanotechnology* **2007,** *18*, 335301.
27. Vazquez-Mena, O.; Villanueva, G.; Savu, V.; Sidler, K.; van den Boogaart, M. A. F.; Brugger, J. Metallic Nanowires by Full Wafer Stencil Lithography. *Nano Lett.* **2008,** *8*, 3675–3682.
28. Savu, V.; Neuser, S.; Villanueva, G.; Vazquez-Mena, O.; Sidler, K.; Brugger, J. Stenciled Conducting Bismuth Nanowires. *J. Vac. Sci. Technol., B* **2010,** *28*, 169–172.
29. Fostner, S.; Burke, S. A.; Topple, J.; Mativetsky, J. M.; Beerens, J.; Grutter, P. Silicon Nanostencils with Integrated Support Structures. *Microelectron. Eng.* **2010,** *87*, 652–657.
30. Yan, X. M.; Contreras, A. M.; Koebel, M. M.; Liddle, J. A.; Somorjai, G. A. Parallel Fabrication of Sub-50-nm Uniformly Sized Nanoparticles by Deposition through a Patterned Silicon Nitride Nanostencil. *Nano Lett.* **2005,** *5*, 1129–1134.
31. Arcamone, J.; van den Boogaart, M. A. F.; Serra-Graells, F.; Fraxedas, J.; Brugger, J.; Perez-Murano, F. Full-Wafer Fabrication by Nanostencil Lithography of Micro/Nanomechanical Mass Sensors Monolithically Integrated with CMOS. *Nanotechnology* **2008,** *19*, 305302.
32. Vazquez-Mena, O.; Sannomiya, T.; Tosun, M.; Villanueva, G.; Voros, J.; Brugger, J. *Analysis and Applications of Nanostructures Created by Stencil Lithography*, Proceedings of the Solid-State Sensors, Actuators and Microsystems Conference (Transducers'09), Denver, CO; June 21−25, 2009; pp 465−468.
33. Aksu, S.; Yanik, A. A.; Adato, R.; Artar, A.; Huang, M.; Altug, H. High-Throughput Nanofabrication of Infrared Plasmonic Nanoantenna Arrays for Vibrational Nanospectroscopy. *Nano Lett.* **2010,** *10*, 2511–2518.
34. Wood, M. A. Colloidal Lithography and Current Fabrication Techniques Producing In-Plane Nanotopography for Biological Applications. *J. R. Soc., Interface* **2007,** *4*, 1–17.
35. Vázquez-Mena, O.; Villanueva, G.; van den Boogaart, M. A. F.; Savu, V.; Brugger, J. Reusability of Nanostencils for the Patterning of Aluminum Nanostructures by Selective Wet Etching. *Microelectron. Eng.* **2008,** *85*, 1237–1240.
36. Vazquez-Mena, O.; Sidler, K.; Savu, V.; Park, C. W.; Villanueva, L. G.; Brugger, J. Reliable and Improved Nanoscale Stencil Lithography by Membrane Stabilization, Blurring and Clogging Corrections. *IEEE Trans. Nanotechnol.* DOI: 10.1109/TNANO.2010.2042724.
37. Lishchynska, M.; Bourenkov, V.; van den Boogaart, M. A. F.; Doeswijk, L.; Brugger, J.; Greer, J. C. Predicting Mask Distortion, Clogging and Pattern Transfer for Stencil Lithography. *Microelectron. Eng.* **2007,** *84*, 42–53.
38. Vazquez-Mena, O.; Villanueva, L. G.; Savu, V.; Sidler, K.; Langlet, P.; Brugger, J. Analysis of the Blurring in Stencil Lithography. *Nanotechnology* **2009,** *20*, 415303.
39. van den Boogaart, M. A. F.; Doeswijk, L. M.; Brugger, J. Silicon-Supported Membranes for Improved Large-Area and High-Density Micro/Nanostencil Lithography. *J. Microelectromech. Syst.* **2006,** *15*, 1663–1670.
40. Arcamone, J.; Sanchez-Amores, A.; Montserrat, J.; van den Boogaart, M. A. F.; Brugger, J.; Perez-Murano, F. Dry Etching for the Correction of Gap-Induced Blurring and Improved Pattern Resolution in Nanostencil Lithography. *J. Micro/Nanolithogr., MEMS, MOEMS* **2007,** *6*, 013005-7.
41. Sidler, K.; Villanueva, G.; Vazquez-Mena, O.; Brugger, J. *Minimized Blurring in Stencil Lithography Using a Compliant Membrane*, Proceedings of the Solid-State Sensors, Actuators and Microsystems Conference (Transducers'09), Denver, CO; June 21−25, 2009; pp 1612−1615.
42. Couderc, S.; Blech, V.; Kim, B. New Surface Treatment and Microscale/Nanoscale Surface Patterning Using Electrostatically Clamped Stencil Mask. *Jpn. J. Appl. Phys.* **2009,** *48*, 095007.
43. Racz, Z.; Seabaugh, A. Characterization and Control of Unconfined Lateral Diffusion under Stencil Masks. *J. Vac. Sci. Technol., B* **2007,** *25*, 857–861.
44. Horcas, I.; Fernandez, R.; Gomez-Rodriguez, J. M.; Colchero, J.; Gomez-Herrero, J.; Baro, A. M. WSXM: A Software for Scanning Probe Microscopy and a Tool for Nanotechnology. *Rev. Sci. Instrum.* **2007,** *78*, 013705.
45. Sannomiya, T.; Hafner, C.; Voros, J. Shape-Dependent Sensitivity of Single Plasmonic Nanoparticles for Biosensing. *J. Biomed. Opt.* **2009,** *14*, 6.
46. Danckwerts, M.; Novotny, L. Optical Frequency Mixing at Coupled Gold Nanoparticles. *Phys. Rev. Lett.* **2007,** *98*, 026104-4.
47. Lamprecht, B.; Schider, G.; Lechner, R. T.; Ditlbacher, H.; Krenn, J. R.; Leitner, A.; Aussenegg, F. R. Metal Nanoparticle Gratings: Influence of Dipolar Particle Interaction on the Plasmon Resonance. *Phys. Rev. Lett.* **2000,** *84*, 4721.
48. Zhao, L.; Kelly, K. L.; Schatz, G. C. The Extinction Spectra of Silver Nanoparticle Arrays: Influence of Array Structure on Plasmon Resonance Wavelength and Width. *J. Phys. Chem. B* **2003,** *107*, 7343–7350.
49. Fischer, H.; Martin, O. J. F. Engineering the Optical Response of Plasmonic Nanoantennas. *Opt. Express* **2008,** *16*, 9144–9154.

50. Jain, P. K.; El-Sayed, M. A. Plasmonic Coupling in Noble Metal Nanostructures. *Chem. Phys. Lett.* **2010,** *487*, 153–164.
51. Lide, D. R. *CRC Handbook of Chemistry and Physics*, 87th ed.; CRC Press: Boca Raton, FL, 2006.
52. Jung, L. S.; Campbell, C. T.; Chinowsky, T. M.; Mar, M. N.; Yee, S. S. Quantitative Interpretation of the Response of Surface Plasmon Resonance Sensors to Adsorbed Films. *Langmuir* **1998,** *14*, 5636–5648.
53. Willets, K. A.; Van Duyne, R. P. Localized Surface Plasmon Resonance Spectroscopy and Sensing. *Annu. Rev. Phys. Chem.* **2007,** *58*, 267–297.
54. Hafner, C. Boundary Methods for Optical Nano Structures. *Phys. Status Solidi B* **2007,** *244*, 3435–3447.
55. Huang, N.-P.; Voros, J.; De Paul, S. M.; Textor, M.; Spencer, N. D. Biotin-Derivatized Poly(L-lysine)-*g*-Poly(ethylene glycol): A Novel Polymeric Interface for Bioaffinity Sensing. *Langmuir* **2002,** *18*, 220–230.